An elastoplastic model for cohesionless soils over a wide stress range

Linlong Mu[1,2], *Shunwei* Wang[1,2*], *Guangming* Yu[3]

[1] Department of Geotechnical Engineering, Tongji University, Shanghai, China
[2] State Key Laboratory of Disaster Reduction in Civil Engineering, Tongji University, Shanghai, China
[3] Institute of Science and Technology, China Three Gorges Corporation, Beijing, China

1 Introduction

With the rapid development of deep underground infrastructure, such as deep tunnels, high-rise building foundations, and underground energy storage facilities, soils are increasingly subjected to high confining pressures. High confining pressure not only significantly alters the strength, stiffness, and volumetric deformation characteristics of granular soils, but may also induce particle breakage, gradation reconfiguration, and pore-structure evolution, causing their macroscopic mechanical response to differ from that under conventional confining pressure conditions [1]. Consequently, in deep engineering applications, reliable characterization of the constitutive behavior of granular soils is critical to stability analyses and deformation predictions.

However, most existing constitutive models for granular soils have been developed primarily for conventional confining pressures [2-5]. This often leads to prediction errors when these models are applied under high confining pressure conditions, because they may not adequately reflect the pressure dependence of the hardening law. In recent years, various enhancements have been proposed to better represent the mechanical behavior of granular soils under high confinement. For example, Russell and Khalili [6] formulated a critical-state relation composed of three linear segments and, on this basis, developed a corresponding bounding-surface constitutive model; Liu et al· [7] found that particle breakage would cause CSL to move according to experiments, so that they developed a CSL expression considering particle breakage and formulated an elastoplastic constitutive model of coral sand. Xiao et al. [8] incorporated a particle breakage parameter into the plastic modulus and developed a constitutive model for sands applicable to high-pressure conditions. Although the above models can predict the stress–strain behavior of sands over a wide range of stresses, the large number of parameters and the difficulty in determining them limit their practical application.

To this end, this study proposes a simplified S-shaped normal compression line (NCL) to avoid predicting a negative void ratio. Subsequently, within the framework of the Modified Cam Clay (MCC) model, two parameters are introduced to correct the geometry of the yield surface. On this basis, an elastoplastic constitutive model for granular soils that is applicable across different pressure levels is established and validated against experimental data.

2 Constitutive model

2.1 Normal compression line

In cohesionless soils, the compression curve generally exhibits an S-shaped form in the $e - lnp$ space. To improve engineering applicability, a simple S-shaped function is adopted to describe the normal compression line (NCL), without introducing additional variables such as a particle breakage index.

$$\ln(e - e_{\mathrm{L}}) = \ln(e_{\Gamma} - e_{\mathrm{L}}) - \lambda p^{n} \tag{1}$$

Similarly, the unloading line can be expressed as:

$$\ln(e - e_{\mathrm{L}}) = \ln(e_{\Gamma} - e_{\mathrm{L}}) - \kappa p^{n} \tag{2}$$

where λ and κ are the slopes of the loading and unloading curves in the $\ln(e - e_{\mathrm{L}}) - p^{n}$ space, respectively. The parameter n controls the curve shape. e_{Γ} and e_{L} denote the void ratio at p= 0 and the limiting void ratio, respectively.

By differentiating Equations (1) and (2), the increment in void ratio can be obtained as:

$$de = -\lambda(e - e_{L})np^{n-1}dp \tag{3}$$

while the increment of elastic void ratio is:

$$de^{e} = -\kappa(e - e_{L})np^{n-1}dp \tag{4}$$

Therefore, the elastic modulus can be expressed as:

$$E = \frac{3(1-2v)(1+e_0)}{\kappa(e-e_L)np^{n-1}} \tag{5}$$

where v denotes Poisson's ratio, e_0 denotes the initial void ratio of the soil specimen.

* Corresponding author: shunweiwang@tongji.edu.cn

Subtracting Equation (4) from Equation (3) yields the increment of plastic void ratio:

$$de^p = (\kappa - \lambda)(e - e_L)np^{n-1}dp \tag{6}$$

2.2 Yield function

In this study, an additional shape correction parameter α is introduced following the model of Yao et al. [9] to better capture the influence of material properties on the yield surface. The modified yield function is expressed as follows:

$$f = \frac{\alpha\eta^2}{M^2-\chi\eta^2} + 1 - \frac{p_x}{p} = 0 \tag{7}$$

where $\eta = q/p$, M denotes the critical state stress ratio, and α and χ govern the yield surface shape.

Using the plastic volumetric strain as the hardening parameter, integrating Eq. (6) yields an integral form of the hardening term; combining it with Eq. (7) gives:

$$f = \left[\left(\frac{\alpha q^2}{p^2M^2-\chi q^2} + 1\right)p\right]^n - \int \frac{(1+e_0)}{(\lambda-\kappa)(e-e_L)} d\varepsilon_v^p - p_{xo}^n \tag{8}$$

Following Yao et al. [10], a stress path correction factor is introduced. The modified hardening variable H is given by:

$$H = \int \frac{(1+e_0)}{(\lambda-\kappa)(e-e_L)} \frac{M_f^4}{M_c^4} \frac{M_c^4-\eta^4}{M_f^4-\eta^4} d\varepsilon_v^p \tag{9}$$

where M_f is the potential strength ratio, and M_c is the phase transformation stress ratio, which is expressed as

$$M_c = M\exp\left(-m \cdot \xi\right) \tag{10}$$

By replacing the plastic volumetric strain term with the modified hardening variable H, the final expression of the yield function can be obtained:

$$f = \left[\left(\frac{\alpha q^2}{p^2M^2-\chi q^2} + 1\right)p\right]^n - H - p_{xo}^n \tag{11}$$

In the numerical implementation, a small positive lower bound p_{min} is introduced, and $p^* = \max\left(p, p_{min}\right)$ is used instead of p in the p^n term to avoid numerical difficulties when the trial mean effective stress becomes slightly negative.

The dynamic densification function R is defined as the ratio of the mean effective stress on the current yield surface to that on the potential yield surface at the same stress ratio η:

$$R = \frac{p}{\bar{p}} = \frac{q}{\bar{q}} \tag{12}$$

Assuming that the potential yield surface has the same form as Eq. (8), combining it with Eq. (12) yields:

$$R = \sqrt[n]{-\frac{\ln\left(e-e_L\right)}{(\lambda-\kappa)} + \bar{p}_{xo}^n} \Big/ \left(\frac{\alpha p\eta^2}{M^2-\chi\eta^2} + p\right) \tag{13}$$

Accordingly, M_f can be expressed as

$$M_f = \frac{M\bar{p} - M_h(\bar{p}-p)}{p} = \left(\frac{1}{R} - 1\right)(M - M_h) + M \tag{14}$$

2.3 State parameter

The state parameter can be defined as the difference between the void ratio e_η corresponding to the constant stress-ratio line at the current stress state and the current void ratio e [10].

$$\xi = e_\eta - e \tag{15}$$

The void ratio e_η corresponding to the constant stress-ratio line at the current stress state can be expressed as:

$$e_\eta = (e_{\mathrm{A}} - e_{\mathrm{L}})\exp\left\{-(\lambda-\kappa)\left[\left(\frac{\alpha p\eta^2}{M^2-\chi\eta^2} + p\right)^n - p^n\right]\right\} + e_{\mathrm{L}} \tag{16}$$

2.4 Plastic potential function

A non-associated flow rule is adopted in this study to decouple the yield condition from the flow rule, and the plastic flow is governed by the plastic potential function (g).

$$g = \ln\frac{p}{p_x} + \ln\left(1 + \frac{q^2}{M_c^2p^2}\right) \tag{17}$$

3 Model prediction

A series of drained [11] and undrained [12] triaxial compression tests were conducted on Cambria sand over a wide stress range. The model parameters are listed in Table 1. Figure 1 presents the predicted results for the drained triaxial tests. As shown in Figure 1, the drained shear response of Cambria sand exhibits strain hardening under different confining pressures, with the deviator stress q gradually approaching a stable level as the axial strain ε_1 increases. Moreover, a higher confining pressure leads to a higher overall stress level. Over a wide range of confining pressures, the model predictions are in good overall agreement with the experimental data.

Figure 2 compares the experimental data with the model predictions for Cambria sand under undrained triaxial compression. As shown in Figure 2, under different confining pressures, the model reasonably captures the general trend of the stress paths in the $p-q$ plane and the variation in pore water pressure. In addition, the deviator stress q increases rapidly with ε_1 and reaches a peak at a relatively small strain. This is followed by strain softening and a gradual approach to a stable value. Both the peak strength and the stabilized strength increase with confining pressure. However, in the 6.4 MPa undrained test, the measured stress path shows a transition from contractive to dilative behavior at the later stage of shearing, whereas the model prediction remains mainly contractive. This indicates that the simplified plastic potential function and hardening formulation still have some limitations in capturing undrained dilatancy under high confining pressure. This issue will be further addressed in future work. Overall, the model demonstrates acceptable predictive capability for the undrained response of Cambria sand.

Additionally, the predictive accuracy of the proposed model is comparable to that of the model by Feng et al.'s model [13]. However, the proposed model involves only 11 parameters, fewer than the 15 parameters in Feng et al. [13], thereby reducing the calibration effort while maintaining predictive performance and facilitating engineering applications.

Table 1. Material parameters of Cambria sand.

λ	κ	m	n	v	M	M_h	e_L	e_Γ	α	χ
0.0129	0.0036	2	1.02	0.3	1.45	1.4	0.10	0.52	3.0	0.4

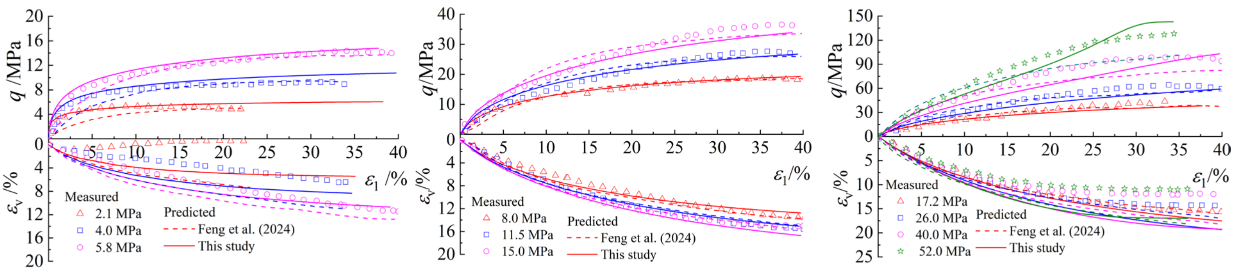

(a) (b) (c)

Figure 1. Comparison between measured and predicted drained triaxial compression responses of Cambria sand. (a)–(c) stress-strain relations and volumetric strains responses.

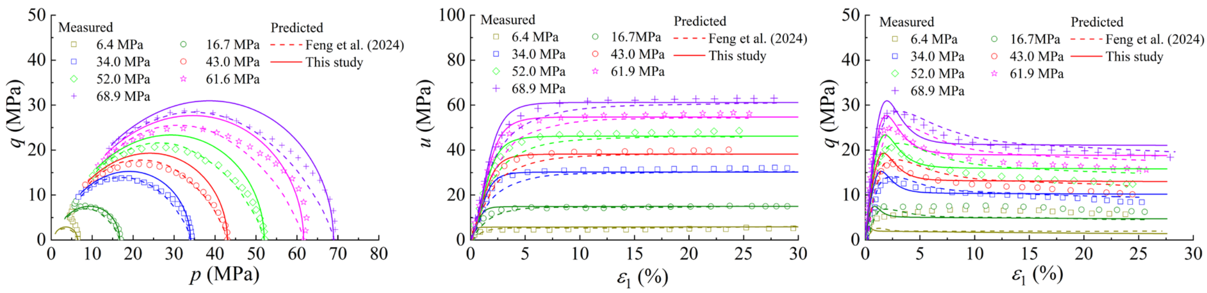

(a) (b) (c)

Figure 2. Comparison between measured and predicted undrained triaxial compression responses of Cambria sand: (a) stress paths in the p - q plane; (b) pore water pressure u versus axial strain ε_1; (c) deviator stress q versus axial strain ε_1.

4 Conclusions

This study proposes a simplified elastoplastic constitutive model applicable over a wide range of confining pressures. First, a simplified S-shaped NCL is introduced to capture the nonlinear evolution of the compression curve and avoid unrealistic negative void ratios. Second, within the MCC yield-function framework, two geometric correction parameters are incorporated to establish a modified yield function; meanwhile, a densification function and a stress-path correction factor are introduced to reduce stress-path dependence. Finally, the predictive capability of the model is validated against drained and undrained triaxial test data. The results show that the proposed model can well predict the stress–strain response, volumetric deformation, and pore-pressure evolution under different confining pressure levels.

References

1. A. Zhang, Y.F. Dafalias, D. Wang, SANISAND-CH: A high-pressure bounding surface model for cemented sand, including methane hydrate-bearing sediments. Comput. Geotech. **179**, 106986 (2025). https://doi.org/10.1016/j.compgeo.2024.106986
2. Z. Gao, J. Zhao, Constitutive modeling of artificially cemented sand by considering fabric anisotropy. Computers and Geotechnics **41**, 57-69 (2012). https://doi.org/10.1016/j.compgeo.2011.10.007
3. J.P. Doherty, D.M. Wood, A bonding and damage constitutive model for lightly cemented granular material. Comput. Geotech. **127**, 103732 (2020). https://doi.org/10.1016/j.compgeo.2020.103732
4. K. Jiao, C. Zhou, A bounding surface model for cemented soil at small and large strains. J. Geotech. Geoenviron. Eng. **150** (2), 04023136 (2024). https://doi.org/10.1061/JGGEFK.GTENG-11604
5. Y. Xiao, Z. Zhang, A.W. Stuedlein, T.M. Evans, Liquefaction modeling for biocemented calcareous sand. J. Geotech. Geoenviron. Eng. **147** (12), 04021149 (2021). https://doi.org/10.1061/(ASCE)GT.1943-5606.0002666
6. A.R. Russell, N. Khalili, Bounding surface plasticity model for sands exhibiting particle crushing. Can. Geotech. J. **41** (6), 1179-1192 (2004). https://doi.org/10.1139/T04-065
7. R.M. Liu, H.Y. Hou, Y.Y. Chen, et al., Elastoplastic constitutive model of coral sand considering particle breakage based on unified hardening parameter. Mar. Georesour. Geotechnol. **40** (6), 655-667 (2022). https://doi.org/10.1080/1064119X.2021.1924321
8. Y. Xiao, C. Wang, Z. Zhang, H. Liu, Z. Yin, Constitutive modeling for two sands under high pressure. Int. J. Geomech. **21** (5), 04021042 (2021). https://doi.org/10.1061/(ASCE)GM.1943-5622.0001987
9. Y.P. Yao, L. Liu, T. Luo, Y. Tian, J.M. Zhang, Unified hardening (UH) model for clays and sands. Comput. Geotech. **110**, 326-343 (2019). https://doi.org/10.1016/j.compgeo.2019.02.024
10. Y.P. Yao, T. Luo, W. Hou, Soil constitutive models (China Communications Press Co., Ltd., Beijing, 2018).
11. J.A. Yamamuro, P.V. Lade, Drained sand behavior in axisymmetric tests at high pressures. J. Geotech. Eng. **122** (2), 109-119 (1996). https://doi.org/10.1061/(ASCE)0733-9410(1996)122:2(109)
12. P.V. Lade, J.A. Yamamuro, Undrained sand behavior in axisymmetric tests at high pressures. J. Geotech. Eng. **122** (2), 120-129 (1996). https://doi.org/10.1061/(ASCE)0733-9410(1996)122:2(120)
13. S. Feng, T. Li, T. Zhang, Elastoplastic modeling for crushable sands over a large stress range based on the particle rearranging and crushing state. J. Eng. Mech. **150** (9), 04024063 (2024). https://doi.org/10.1061/JENMDT.EMENG-7836